

Hybrid nanocolloids with programmed three-dimensional shape and material composition

Andrew G. Mark[†], John G. Gibbs[†], Tung-Chun Lee and Peer Fischer[★]

Tuning the optical^{1,2}, electromagnetic^{3,4} and mechanical properties of a material requires simultaneous control over its composition and shape⁵. This is particularly challenging for complex structures at the nanoscale because surface-energy minimization generally causes small structures to be highly symmetric⁵. Here we combine low-temperature shadow deposition with nanoscale patterning to realize nanocolloids with anisotropic three-dimensional shapes, feature sizes down to 20 nm and a wide choice of materials. We demonstrate the versatility of the fabrication scheme by growing three-dimensional hybrid nanostructures that contain several functional materials with the lowest possible symmetry, and by fabricating hundreds of billions of plasmonic nanohelices, which we use as chiral metafluids with record circular dichroism and tunable chiroptical properties.

At the nanoscale it has long been realized that shape and material composition directly influence function. The optical properties of plasmonic metals are, for instance, defined by the nanoparticle's shape and can be tuned by changing its dimensions and aspect ratio^{1,2}. Shape also controls the magnetic anisotropy and the critical grain size of magnetic nanostructures³, and influences catalytic activity⁶. Equally important is the choice of material, which for instance dictates the hardness of a magnet⁷ or the yield stress of a mechanical spring. Selected complex inorganic nanoshapes have been obtained through wet chemical or supramolecular routes^{8–10}, template-assisted growth^{11,12}, nanoscale carving¹³, on-wire lithography¹⁴ and scanning probe lithography¹⁵. However, whereas combined control of material and shape is a cornerstone of engineering and manufacturing at the macroscale, this control is difficult to exercise at the nanoscale within one general fabrication method. Here, we demonstrate a parallel fabrication scheme for nanostructures with programmed shape and composition that cannot be synthesized by any existing method. We grow nanoparticles with complex three-dimensional (3D) morphologies that contain a number of different functional materials using a physical vapour deposition process that combines independent control over the nanoseed pattern, substrate manipulation and temperature. The versatility of the method has allowed us to create metafluids whose chiroptical responses can be tuned through the visible regime. In one wafer run we are able to obtain high yields of anisotropic nanocolloids that contain magnetic, semiconducting, metallic and insulating materials within the same structure.

The fabrication scheme is depicted in Fig. 1. First, a uniform hexagonal array of Au nanodots is deposited onto a Si

wafer by micellar nanolithography (Fig. 1a), in which gold-loaded self-assembled polystyrene-*b*-poly[2-vinylpyridine (HAuCl₄)] diblock copolymer micelles are transferred as uniform monolayer films onto the wafer by spin-coating^{16,17}. Plasma treatment removes the polymer and reduces the gold salt, and leaves behind the regular gold nanodot array seen in Fig. 1a. The spacing and size of the Au dots can be adjusted by changing the polymer molecular weight, Au loading, and spin-coating speed (see Methods and Supplementary Information for further details). This technique allows facile and rapid wafer-scale patterning with feature sizes smaller than what is possible with nanoimprint lithography, and with processing times orders of magnitude faster than electron-beam lithography.

In the next stage (Fig. 1b) material is deposited onto the substrate by physical vapour deposition at grazing incidence. The nanodots act as seeds onto which the incoming evaporant deposits and grows in a columnar fashion. As expanded on below, the seed size directly affects the lateral dimensions of the resultant nanostructures. The uniformity of the seeds leads to improved homogeneity among the grown nanostructures. Manipulating the tilt and rotation of the substrate relative to the incoming vapour flux controls the morphology of the growing structures^{18–20}; for instance, fabricating a one-turn helix requires one full rotation of the substrate during the deposition. The technique is also known as shadow-growth or glancing-angle deposition and has achieved great success in fabricating microscale structures and thin solid films of controlled porosity^{20–22}. This is sufficient for many materials at the microscale, but evaporants with high surface mobilities, for example noble metals, pose a particular challenge at the nanoscale, as here the adatoms simply diffuse during growth, and yield low-energy equilibrium shapes with high symmetry. We address this problem by cooling the substrate, where necessary, to kinetically preserve the shape determined by the growth programme (Supplementary Information). The combination of uniform nanoseeding and low-temperature growth is crucial for ensuring the fidelity of the nanostructures, as illustrated by a series of Au structures grown under various conditions (Supplementary Fig. S1). If in addition the evaporant flux composition is varied during growth, it then becomes possible to create complex hybrid structures: in the example of Fig. 1c, a nanohook made from Al₂O₃, Ti and Cu (transmission electron microscopy (TEM) image in Fig. 1d and model in Fig. 1e). A three-inch wafer contains roughly 10¹¹ such nanoparticles, and can be grown in approximately one hour. The nanocolloids may be functionalized on wafer before being released into solution by sonication. For instance, in this work we stabilized Au nanoparticles with 1 mM sodium citrate. Releasing the particles

Max Planck Institute for Intelligent Systems, Heisenbergstraße 3, 70569 Stuttgart, Germany. [†]These authors contributed equally to this work.

*e-mail: fischer@is.mpg.de

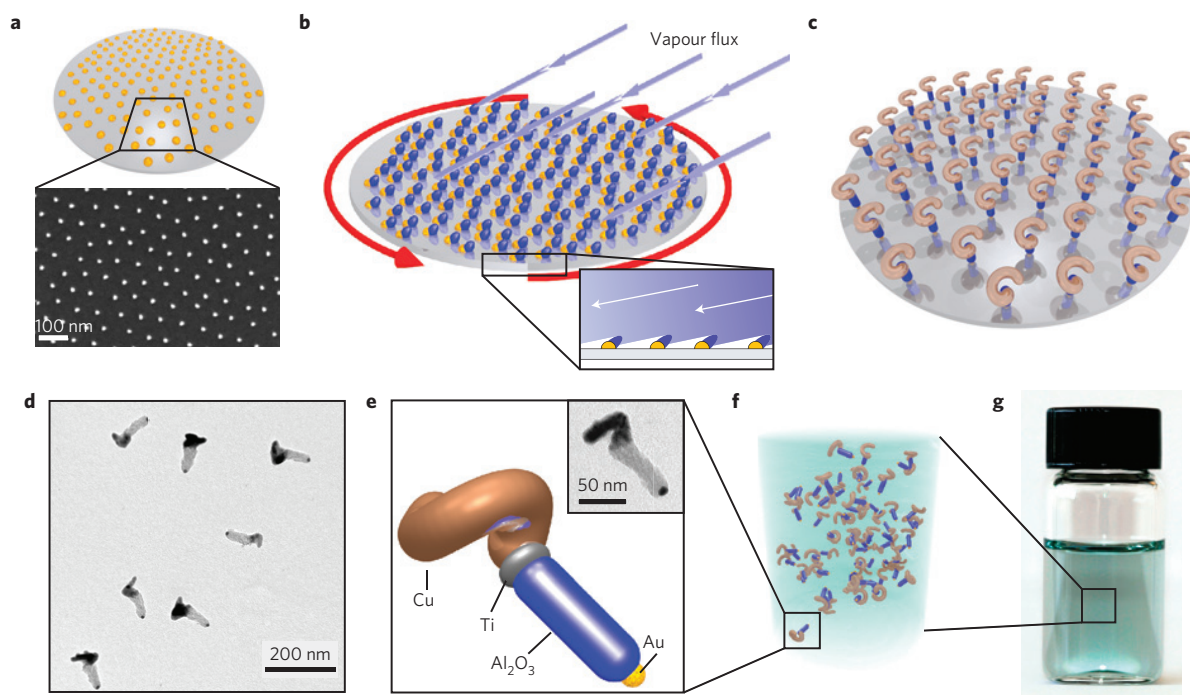


Figure 1 | Fabrication scheme illustrated for nanohooks with C_1 symmetry. **a,b**, The 14 nm gold nanodots patterned by micellar nanolithography (**a**; bottom, SEM image of patterned wafer) act as nucleation sites (**b**) during subsequent shadow growth. **c**, Manipulation of the substrate angle and deposition material creates complex 3D structures. The growth process takes approximately 1 h. **d**, TEM image of hybrid insulator-metal nanohooks. **e**, Model of the designed structure, and TEM image showing the grown structure (inset). **f,g**, On sonication the nanoparticles are released into solution (schematic (**f**), photograph (**g**)).

from the wafer yields a colloidal suspension suitable for further experiments (Fig. 1f,g). The high fidelity of the structures means that no purification steps are generally required.

The size and in particular the lateral dimension of the nanostructures is a function of the size of the seed particles on which the nanostructures grow. Figure 2 shows SiO_2 rods grown on 14–36 nm Au/Ag nanodot seeds (see Supplementary Information for details on the nanodot enhancement). After growth, the structures were lifted off into suspension and the distribution of diameters was measured by TEM imaging. The results, based on measurements of over 100 nanoparticles of each population, show a clear correlation between increasing seed size and larger diameter. Thus, the lateral dimension of nanoparticles grown with this technique is a function of the seed size, and small structures require correspondingly small seeds. Micellar nanolithography can provide seeds as small as 6 nm.

Figure 3 shows tailored hybrid nanocolloids with combinations of multiple functional materials and shape control (further images in Supplementary Figs S6–S8). The nano-barcodes (point group symmetry $C_{\infty v}$ in Schönflies notation)^{23,24}, nano-zigzags (C_s) and nanohooks (C_1) are non-centrosymmetric and have progressively lower symmetry. Statistical analysis of the nanocolloids reveals that excellent control over the dimensions has been achieved for the structures, with a standard deviation of the feature sizes in the direction of growth of $\sim 10\%$, and of $\sim 20\%$ orthogonal to the growth direction, as well as a good control over the relative angles, with $\theta = 75 \pm 6^\circ$ and $\varphi = 66 \pm 6^\circ$ (Fig. 3 top row; see Supplementary Note S10 and Tables S3–S7). Furthermore, each particle contains several functional materials, including insulators, metals, semiconductors and magnetic materials, incorporated in a single structure. Energy-filtered TEM (EF-TEM) confirms the designed elemental distribution within each nanocolloid (Fig. 3, row 3). The nanohooks consist of an aluminium oxide rod (with an embedded gold nano-seed), a titanium adhesion layer and a

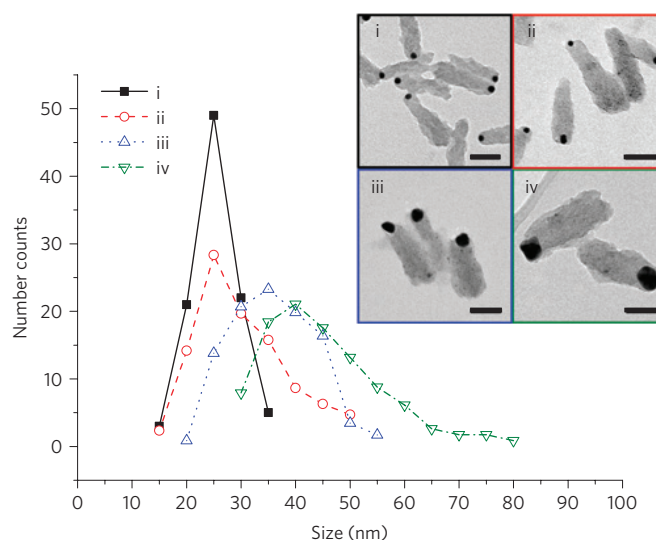


Figure 2 | Seed size controls the nanostructure's diameter. The histogram shows the distribution of rod diameters for SiO_2 nanorods grown on seeds of diameter 14 nm (i), 17 nm (ii), 29 nm (iii) and 36 nm (iv). At least 100 nanoparticles were measured for each sample. Plots were normalized (total population = 100) for convenient comparison. The inset shows the corresponding TEM images. Scale bars, 50 nm.

one-turn copper helix (Fig. 3 right column, and Supplementary Fig. S5), which imparts chirality. An aqueous solution of the nanohooks is shown in Fig. 1g. As the solution is prepared through a template- and surfactant-less approach, it allows convenient on-wafer chemical functionalization of the immobilized particles before release, without the need to address colloidal stability or purification (Supplementary Fig. S7). A potential application of

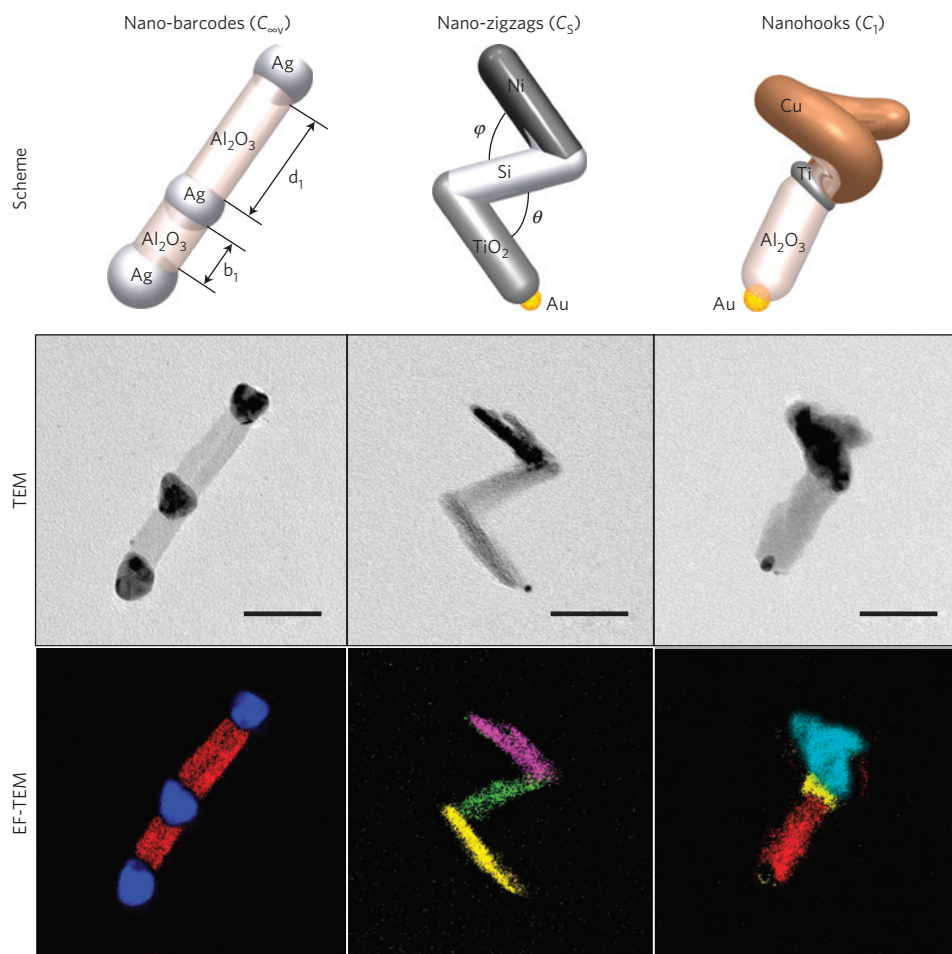


Figure 3 | Hybrid nanoparticles with progressively lower symmetry. Columns from left to right show: $C_{\infty v}$ nano-barcodes, C_3 nano-zigzags combining magnetic, semiconducting and insulating materials, and the lowest possible symmetry C_1 nanohooks with defined chirality. First row, structure models. TEM images (second row) and false-colour elemental maps (third row) of the same regions generated by analysing EF-TEM images using the three-window technique (Supplementary Note S9). Colour code (and corresponding core-loss edges): red, aluminium (Al $L_{2,3}$ for nano-barcodes, Al K for nanohooks); blue, silver (Ag $M_{4,5}$); yellow, titanium (Ti $L_{2,3}$); green, silicon (Si $L_{2,3}$); purple, nickel (Ni $L_{2,3}$); cyan, copper (Cu $L_{2,3}$).

anisotropic particles with chemical functionalities is nanoscale assembly⁵, and to the best of our knowledge low-symmetry nanostructures with multiple functionalities and defined chirality have not yet been demonstrated with other fabrications schemes. These should enable investigations into assembly phenomena such as chiral conglomerate and racemate formation, which have hitherto been limited to only molecular or soft-material systems.

We use this control over shape and composition to address an application in the field of plasmonic metamaterials, which requires structures with sizes smaller than the wavelength of light. Herein, we grow ~ 10 mg of enantiopure Au nanohelices as plasmonic chiral light antennas. Statistical analysis of TEM images (Fig. 4b, and Supplementary Fig. S4 and Tables S3 and S4) confirms that the helices have two turns, a pitch of 34 nm and an overall height of 100 ± 8 nm. They are ~ 40 times smaller than the ones fabricated as broadband infrared polarizers using two-photon lithography²⁵, and are smaller than the near-infrared stereometamaterials grown by electron-beam lithography⁴. Thus, such nanohelices are expected to show optical activity at visible wavelengths. The growth of Au helices at the sub-100 nm scale has only recently been achieved through the elegant self-assembly of gold nanoparticles with DNA origami²⁶. An advantage of the present scheme is that the critical helix parameters of height, pitch and chiral sense are selected during growth, and can be readily adjusted. Furthermore, we can readily incorporate other materials including alloys (see below).

After growth we remove the nanohelices from the substrate and suspend them into a 1 mM aqueous solution of sodium citrate by sonicating a ~ 1 cm² wafer piece. The circular dichroism spectra of the resulting metafluids (Fig. 4b) of nanohelices with left- and right-handed chirality show the distinct Cotton effect predicted for plasmonic chiral nanoparticles^{26–28}. The spectra agree with an analytical quantized one-electron model²⁹ and numerical calculations conducted with the package DDSCAT (ref. 30) shown in Fig. 4d (Methods and Supplementary Information). As expected, the long-wavelength circular dichroism exhibits a positive ellipticity for right-handed helices²⁹. Moreover, the analytical quantum model shows that the spectral peak position is an exquisite function of the radius of the helix, and is thus a very sensitive measure of the quality of the structures (Supplementary Information). The opposite helicities are grown on different patterned wafers and on different runs but show equal circular dichroism spectra with opposite sign. This is a direct measure of the fidelity of the growth technique in reproducibly fabricating complex nanostructures. We attribute the differences in the magnitude of the two solution spectra to concentration mismatch in preparing the colloid suspensions. A control experiment of spectra taken in transmission through thin films of opposite helicities shows good agreement (Supplementary Fig. S3). Figure 4c shows the circular dichroism spectra of two- and one-turn helices grown at 150 K; the circular dichroism spectrum of the one-turn helices has the same sign, shape and peak positions

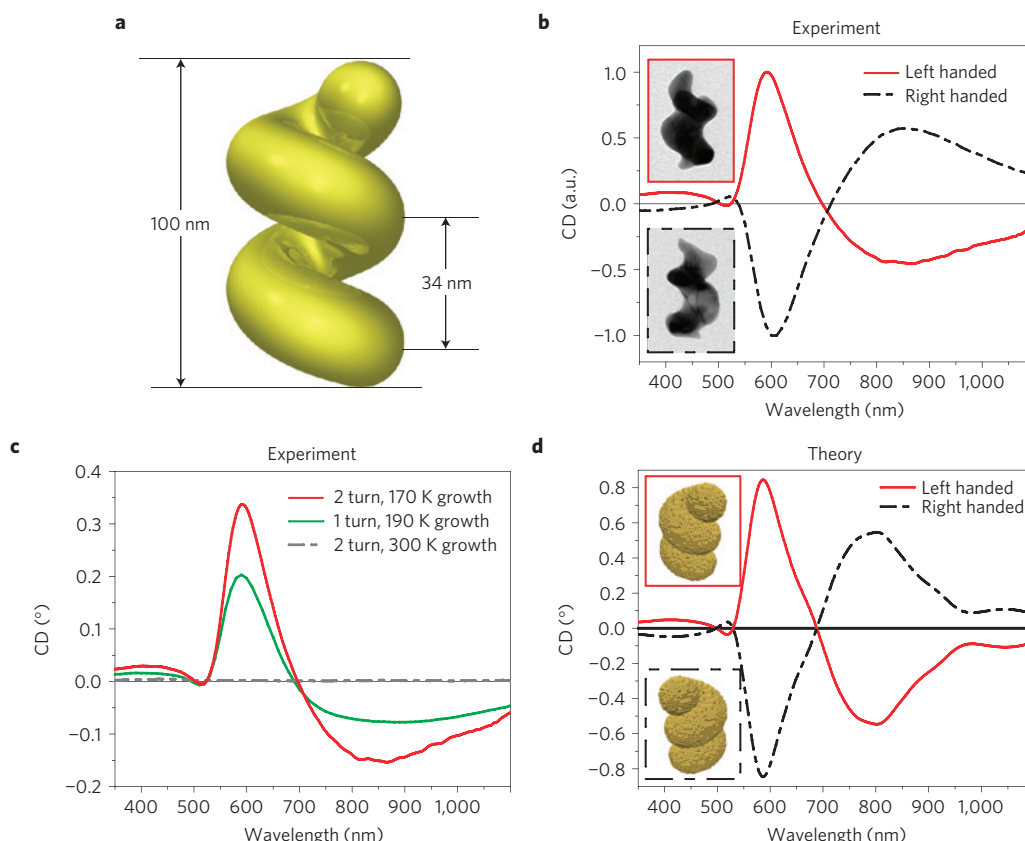


Figure 4 | The chiroptical response of solutions of Au nanohelices. **a**, Model two-turn gold nanohelix showing critical dimensions. **b**, Normalized circular dichroism (CD) spectra of left-handed and right-handed helices. Inset: TEM images of grown structures with left (top) and right (bottom) chirality (image dimensions: 85 nm \times 120 nm). **c**, Circular dichroism spectra of two- and one-turn helices grown under cooling conditions, and of nominal two-turn helices grown at room temperature. The spectra are plotted against an absolute y axis calibrated according to the optical density of the λ_{\max} peaks (at around 600 nm) in the corresponding ultraviolet-visible spectra. **d**, Simulated CD spectra for **a** based on model dimensions taken from TEM images. The insets show the discrete dipole models used in the calculations.

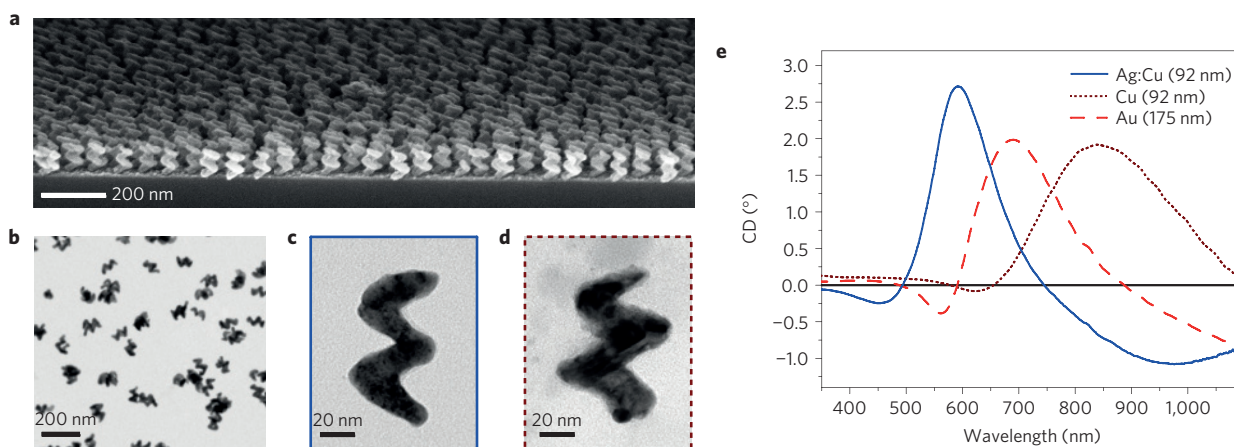


Figure 5 | Tuning the chiroptical response by composition and shape. **a**, Oblique-angle SEM image showing Ag:Cu (65:35) alloy helices as grown on wafer before release. **b**, Wide-field TEM image of the same Ag:Cu helices after deposition from solution onto TEM grid. **c, d**, TEM image of a single Ag:Cu alloy helix (**c**) and a Cu helix (**d**). Both helices are 92 nm tall with two turns. **e**, Suspension circular dichroism (CD) spectra. The CD response can be tailored by controlling the helix composition (Cu versus Ag:Cu alloy helices), and also by the helix size (Au 175 nm tall, two turns). The estimated nanoparticle concentration of Ag:Cu alloy helices is $\sim 10^{-11}$ M (see Supplementary Section S5 for more details).

as that of the two-turn helices, but with a weaker ($\sim 50\%$) signal, in accord with numerical predictions. On the other hand, gold nanoparticles fabricated with the same growth programme but at room temperature (300 K) have poor structure, and consequently exhibit no measurable circular dichroism signal for the resulting

nanocolloidal solution (Fig. 4c, grey line). This illustrates the importance of controlling seed structure and cooling for the design of uniform nanostructures.

Figure 5 demonstrates how changes in shape and material composition within nanostructures let us tune the chiroptical response

of nanohelices across the visible spectrum. Figure 5a–c shows nanohelices grown as a Ag:Cu (65:25) alloy, which have the same shape as the Cu helices in Fig. 5d, but a substantially blueshifted spectral response (Fig. 5e). We note that the Ag:Cu helices are not bimetallic core-shell structures²⁶, but rather a true alloy grown by co-deposition from two independent evaporation sources. In addition to shifting the peak positions of the surface plasmon resonance, alloying will affect the structural and mechanical properties of the nanostructures. On the basis of the nanolithographic seed density we deduce that the particle concentration is of the order of tens of picomolar (details in Supplementary Information) and that the molar ellipticity is at least $[\theta] \sim 10^9 \text{ (M cm)}^{-1}$, which is more than an order of magnitude larger than what has previously been shown²⁶.

This Letter suggests a way to quickly obtain complex nanocolloids with established techniques and in useful numbers that could otherwise not be synthesized with existing methods. The scheme offers control over both the choice of materials and the 3D shape with feature sizes down to 20 nm. We demonstrate the growth of anisotropic designer nanocolloids containing any combination of magnetic, plasmonic, dielectric, (semi)conducting and even alloyed materials. For metafluidic applications we show that the rapid wafer-scale fabrication affords high resolution and unprecedented versatility in realizing nanoparticles with a chiroptical response tunable in the visible. We expect that the ability to construct complex custom shapes that contain demanding materials, such as more reactive metals, and the opportunity for surface functionalization before release, opens up new possibilities for solution-based nanomaterials and nanophotonics. The technique offers a general route to the fabrication of complex 3D nanostructures with tailored electric, magnetic, optical and mechanical properties.

Methods

Block copolymer micellar nanolithography. Au nanodot seed patterns were prepared from polystyrene(1,056)-block-poly(2-vinylpyridine)(495) (Polymer Source) block copolymer in toluene at a concentration of 4 mg ml^{-1} . Gold was added in the form of $\text{HAuCl}_4 \cdot 3(\text{H}_2\text{O})$ at a molar ratio of 0.5 per vinylpyridine unit. This generates spherical inverse micelles with a metal-loaded core. Surface-bound nanodot arrays were deposited on piranha-cleaned Si wafers (Si(100) CrysTec) by spin-coating $50 \mu\text{l}$ of micelle solution at 8,000 r.p.m. for 1 min. Subsequent plasma treatment in a TePla PS210 Microwave Plasma System (W10 (10% H_2 , 90% Ar); 350 W; 0.4 mbar; 45 min) removed the polymer, and reduced and crystallized the Au, leaving behind a quasi-hexagonal array of 14 nm gold nanodots separated by $71 \pm 9 \text{ nm}$ (as measured by scanning electron microscopy (SEM) with an in-lens detector).

Structure growth. The repertoire of shapes that can be grown using glancing-angle deposition shadow growth methods^{20–22} includes columnar rods, zigzag structures, as well smooth and segmented twisted and helical structures, among others. As such it cannot grow for instance, looped shapes, knots or branched structures, and as with any other physical vapour technique, requires materials compatible with vacuum deposition.

For the structures presented in this Letter, depositions were performed with vacuum chamber pressures in the range 10^{-7} – 10^{-6} torr, by electron-beam evaporation. Substrate tilt and rotational rates, $d\phi/dt$, were constantly updated with closed-loop feedback based on measurements of material deposition rates on a quartz-crystal monitor and controlled by a computer running code developed in the laboratory. When growing helices, substrate rotation rates correspond directly to the desired pitch. Wafer cooling is achieved with a custom substrate manipulator that includes an in-vacuum liquid N_2 Dewar that provides heat transfer through the ball bearings and thus permits cooling to as low as -170°C under continuous rotation. Binary alloys were fabricated by co-deposition from two evaporators simultaneously. The alloy stoichiometry was controlled by measuring and controlling the deposition rate from each evaporator independently.

SEM and TEM analysis. Structures were imaged in a Zeiss Gemini SEM on the silicon wafer as grown. Side-view SEM images were acquired by cleaving the wafer to expose a pristine edge. TEM samples were prepared by drop-casting $\sim 5 \mu\text{l}$ of colloidal suspension onto a holey carbon TEM grid (Cu 400 mesh), followed by drying. The sample-loaded TEM grid was then washed (deionized water) to remove excess salts and surfactants, and finally dried. For samples containing copper this procedure was performed under argon atmosphere. Bright-field TEM images were recorded on a Philips CM200 or a Zeiss 912 Omega under an accelerating voltage of 200 kV or 120 kV, respectively. EF-TEM images were recorded on a Zeiss

912 Omega (120 kV) with the appropriate energy slit inserted into the in-column electron energy filter.

Circular dichroism analysis. Circular dichroism spectra were obtained with a Jasco J-810 circular dichroism spectrometer. The cuvette path length was 1 cm. Measurements of ultraviolet–visible absorption were made on a Cary ultraviolet–visible 4000 spectrophotometer.

Numerical simulations. The optical activity of helical gold nanoparticles in suspension was modelled using the DDSCAT implementation of the discrete dipole approximation^{30,31}. Calculations were performed over 70 wavelengths between 350 nm and 1,100 nm. To account for the effect of finite-sized randomly oriented helices in solution, the optical response was averaged over 128 separately calculated target orientations.

Received 6 February 2013; accepted 9 May 2013; published online 23 June 2013

References

- Burda, C., Chen, X., Narayanan, R. & El-Sayed, M. A. Chemistry and properties of nanocrystals of different shapes. *Chem. Rev.* **105**, 1025–1102 (2005).
- Choi, C. L. & Alivisatos, A. P. From artificial atoms to nanocrystal molecules: Preparation and properties of more complex nanostructures. *Annu. Rev. Phys. Chem.* **61**, 369–389 (2010).
- Albrecht, M. *et al.* Magnetic multilayers on nanospheres. *Nature Mater.* **4**, 203–206 (2005).
- Hentschel, M., Schäferling, M., Weiss, T., Liu, N. & Giessen, H. Three-dimensional chiral plasmonic oligomers. *Nano Lett.* **12**, 2542–2547 (2012).
- Glötzer, S. C. & Solomon, M. J. Anisotropy of building blocks and their assembly into complex structures. *Nature Mater.* **6**, 557–562 (2007).
- Linic, S., Christopher, P. & Ingram, D. B. Plasmonic-metal nanostructures for efficient conversion of solar to chemical energy. *Nature Mater.* **10**, 911–921 (2011).
- Sun, S., Murray, C. B., Weller, D., Folks, L. & Moser, A. Monodisperse FePt nanoparticles and ferromagnetic FePt nanocrystal superlattices. *Science* **287**, 1989–1992 (2000).
- Xia, Y., Xiong, Y., Lim, B. & Skrabalak, S. E. Shape-controlled synthesis of metal nanocrystals: Simple chemistry meets complex physics? *Angew. Chem. Int. Ed.* **48**, 60–103 (2009).
- Mann, S. Self-assembly and transformation of hybrid nano-objects and nanostructures under equilibrium and non-equilibrium conditions. *Nature Mater.* **8**, 781–792 (2009).
- Grzybowski, B. A., Wilmer, C. E., Kim, J., Browne, K. P. & Bishop, K. J. M. Self-assembly: From crystals to cells. *Soft Matter* **5**, 1110–1128 (2009).
- Seddon, A. M., Patel, H. M., Burkett, S. L. & Mann, S. Chiral templating of silica–lipid lamellar mesophase with helical tubular architecture. *Angew. Chem. Int. Ed.* **41**, 2988–2991 (2002).
- Sone, E. D., Zubarev, E. R. & Stupp, S. I. Semiconductor nanohelices templated by supramolecular ribbons. *Angew. Chem. Int. Ed.* **41**, 1705–1709 (2002).
- González, E., Arbiol, J. & Puntès, V. F. Carving at the nanoscale: Sequential galvanic exchange and kirkendall growth at room temperature. *Science* **334**, 1377–1380 (2011).
- Qin, L., Park, S., Huang, L. & Mirkin, C. A. On-wire lithography. *Science* **309**, 113–115 (2005).
- Pires, D. *et al.* Nanoscale three-dimensional patterning of molecular resists by scanning probes. *Science* **328**, 732–735 (2010).
- Glass, R., Möller, M. & Spatz, J. P. Block copolymer micelle nanolithography. *Nanotechnology* **14**, 1153–1160 (2003).
- Spatz, J. P. *et al.* Ordered deposition of inorganic clusters from micellar block copolymer films. *Langmuir* **16**, 407–415 (1999).
- Young, N. O. & Kowal, J. Optically active fluorite films. *Nature* **183**, 104–105 (1959).
- Robbie, K., Friedrich, L. J., Dew, S. K., Smy, T. & Brett, M. J. Fabrication of thin films with highly porous microstructures. *J. Vac. Sci. Technol. A* **13**, 1032–1035 (1995).
- Hawkeye, M. M. & Brett, M. J. Glancing angle deposition: Fabrication, properties, and applications of micro- and nanostructured thin films. *J. Vac. Sci. Technol. A* **25**, 1317–1335 (2007).
- Robbie, K., Brett, M. J. & Lakhtakia, A. Chiral sculptured thin films. *Nature* **384**, 616–616 (1996).
- Zhao, Y. P., Ye, D. X., Wang, G. C. & Lu, T. M. in *Nanotubes and Nanowires* 5219 (eds Lakhtakia, A. & Maksimenko, S.) 59–73 (2003).
- Mokari, T., Szturm, C. G., Salant, A., Rabani, E. & Banin, U. Formation of asymmetric one-sided metal-tipped semiconductor nanocrystal dots and rods. *Nature Mater.* **4**, 855–863 (2005).
- Algra, R. E. *et al.* Twinning superlattices in indium phosphide nanowires. *Nature* **456**, 369–372 (2008).
- Gansel, J. K. *et al.* Gold helix photonic metamaterial as broadband circular polarizer. *Science* **325**, 1513–1515 (2009).

26. Kuzyk, A. *et al.* DNA-based self-assembly of chiral plasmonic nanostructures with tailored optical response. *Nature* **483**, 311–314 (2012).
27. Fan, Z. & Govorov, A. O. Chiral nanocrystals: Plasmonic spectra and circular dichroism. *Nano Lett.* **12**, 3283–3289 (2012).
28. Zhang, Z. Y. & Zhao, Y. P. Optical properties of helical and multiring Ag nanostructures: The effect of pitch height. *J. Appl. Phys.* **104**, 013517–013517 (2008).
29. Moore, D. & Tinoco, J. I. The circular dichroism of large helices. A free particle on a helix. *J. Chem. Phys.* **72**, 3396–3400 (1980).
30. Draine, B. T. & Flatau, P. J. Discrete-dipole approximation for scattering calculations. *J. Opt. Soc. Am. A* **11**, 1491–1499 (1994).
31. Bruce, T. & Draine, P. J. F. User Guide for the Discrete Dipole Approximation Code DDSCAT 7.2. arXiv (2012).

Acknowledgements

We are grateful to C. Miksch and J. P. Spatz for providing us with micellar nanolithographically patterned substrates and for SEM access. We thank the Stuttgart

Center for Electron Microscopy for technical support with the TEM imaging. This work was supported by the European Research Council under the ERC Grant agreement 278213.

Author contributions

J.G.G. and A.G.M. built the shadow growth set-up, and grew the nanostructures. T-C.L. prepared the nanocolloidal solutions and carried out the TEM imaging. A.M. undertook numerical calculations. P.F. proposed the experiment, and A.G.M., J.G.G., T-C.L. and P.F. analysed the data and wrote the paper.

Additional information

Supplementary information is available in the [online version of the paper](#). Reprints and permissions information is available online at www.nature.com/reprints. Correspondence and requests for materials should be addressed to P.F.

Competing financial interests

The authors declare no competing financial interests.